NEUROSCIENCE

High-throughput evolution of near-infrared serotonin nanosensors

Sanghwa Jeong[1], Darwin Yang[1], Abraham G. Beyene[1], Jackson Travis Del Bonis-O'Donnell[1], Anneliese M. M. Gest[2], Nicole Navarro[1], Xiaoqi Sun[1], Markita P. Landry[1,3,4,5]*

Copyright © 2019 The Authors, some rights reserved; exclusive licensee American Association for the Advancement of Science. No claim to original U.S. Government Works. Distributed under a Creative Commons Attribution NonCommercial License 4.0 (CC BY-NC).

Imaging neuromodulation with synthetic probes is an emerging technology for studying neurotransmission. However, most synthetic probes are developed through conjugation of fluorescent signal transducers to pre-existing recognition moieties such as antibodies or receptors. We introduce a generic platform to evolve synthetic molecular recognition on the surface of near-infrared fluorescent single-wall carbon nanotube (SWCNT) signal transducers. We demonstrate evolution of molecular recognition toward neuromodulator serotonin generated from large libraries of ~6.9 × 10^{10} unique ssDNA sequences conjugated to SWCNTs. This probe is reversible and produces a ~200% fluorescence enhancement upon exposure to serotonin with a K_d = 6.3 μM, and shows selective responsivity over serotonin analogs, metabolites, and receptor-targeting drugs. Furthermore, this probe remains responsive and reversible upon repeat exposure to exogenous serotonin in the extracellular space of acute brain slices. Our results suggest that evolution of nanosensors could be generically implemented to develop other neuromodulator probes with synthetic molecular recognition.

INTRODUCTION

Optical probes are of fundamental importance for advancing our understanding of biological processes such as neurotransmission. Specifically, serotonin, or 5-hydroxytryptamine (5-HT), is a monoamine neuromodulator that plays diverse roles in the central nervous system and is critically implicated in the etiology and treatment of mood and psychiatric disorders (*1*). 5-HT also plays critical roles in modulating memory and learning (*2*, *3*) and in the regulation of mood (*4*), sleep (*5*), and appetite (*5*). As such, aberrations in 5-HT signaling are thought to underlie multiple mental health disorders including major depressive disorder (*6*), bipolar disorder (*7*), autism (*8*), schizophrenia (*9*), anxiety (*10*), and addiction (*11*). Classical neurotransmission occurs through rapid activation of ligand-gated ion channels in which neurotransmitter signaling is confined at the synaptic cleft and thus to singular synaptic partners (*12*). Conversely, 5-HT acts primarily as a neuromodulator and may undergo signaling through extrasynaptic diffusion, enabling a few neurons to affect broader networks of neuronal activity through 5-HT volume transmission. As such, there is great interest in monitoring the spatial component of 5-HT modulation in addition to its temporal dynamics. Current methods for measuring 5-HT and other neuromodulators include tools adapted from analytical chemistry to measure 5-HT in the brain extracellular space with varying levels of selectivity and spatiotemporal resolution: Fast-scan cyclic voltammetry leverages redox chemistry to enable rapid temporal measurement of 5-HT by inserting a carbon electrode into brain tissue (*13*). Microdialysis is an analytical chemistry method in which fluid samples from brain tissue are subject to downstream analysis with chromatography (*14*). Recently, a field-effect transistor sensor modified with a 5-HT aptamer was reported to exhibit a highly sensitive and selective electrochemical response to 5-HT under physiological conditions (*15*). However, previous methods suffer from limited spatial resolution, and microdialysis sampling occurs on the order of minutes, which precludes assaying fast 5-HT modulatory transients in the brain. While a few optical probes for 5-HT of varying selectivity have been developed, to date, none have been implemented for monitoring 5-HT modulation on spatiotemporal scales relevant to monitoring endogenous 5-HT kinetics (*16*–*21*). This lack of tools to probe the dynamics of neuromodulators such as 5-HT stems from the difficulty in developing synthetic optical probes for extracellular analytes.

To address the challenge of reliable generation of synthetic neuromodulator probes, we describe a generic platform for evolution of molecular selectivity and demonstrate its utility by developing a nanosensor for neuromodulator 5-HT. Our approach entails systematic evolution of ligands by exponential enrichment implemented on single-wall carbon nanotube (SWCNT) surfaces, a process we have termed SELEC. Specifically, our near-infrared 5-HT probe (nIRHT) is developed through nanosensor evolution in which large libraries of more than 10^{10} polynucleotide-SWCNT conjugates are evolved for 5-HT selectivity through iterative enzymatic amplification of 5-HT–selective polymers and deep sequencing to identify unique polynucleotide sequences that confer 5-HT selectivity when pinned to SWCNT surfaces. Molecular recognition and selectivity for 5-HT over its metabolic precursors, 5-HT metabolites, and 5-HT receptor drugs are conferred through surface adsorption of single-stranded polynucleotides to the SWCNT surface. We show that six rounds of polynucleotide-SWCNT evolution enable generation of multiple candidate optical sensors, whereby the best-responding construct from the evolution cohort, nIRHT, is next characterized as a 5-HT optical probe.

We further assess nIRHT for potential use as a 5-HT imaging probe with appropriate spatiotemporal resolution for imaging endogenous 5-HT modulation. nIRHT responds to 5-HT with a change in fluorescence, $\Delta F/F_0$, of up to 194 ± 6% in the nIR fluorescence emission window of 1000 to 1300 nm and is shown to bind 5-HT with a K_d of 6.3 μM (R^2 > 0.99). We further demonstrate that nIRHT is reversible and exhibits unaltered performance in artificial

[1]Department of Chemical and Biomolecular Engineering, University of California, Berkeley, Berkeley, CA 94720, USA. [2]Department of Chemistry, University of California, Berkeley, Berkeley, CA 94720, USA. [3]Innovative Genomics Institute (IGI), Berkeley, CA 94720, USA. [4]California Institute for Quantitative Biosciences, QB3, University of California, Berkeley, Berkeley, CA 94720, USA. [5]Chan Zuckerberg Biohub, San Francisco, CA 94158, USA.
*Corresponding author. Email: landry@berkeley.edu

cerebrospinal fluid (aCSF). Of importance to understanding pharmacology in the context of 5-HT signaling, we show that nIRHT does not respond to 5-HT metabolites of 5-hydroxyindoleacetic acid (HIAA), 5-hydroxytryptophan (HTP), and 5-methoxytryptophan (MTP) and 5-HT receptor-targeting drugs, such as fluoxetine, 3,4-methylenedioxymethamphetamine (MDMA), 25I-NMOMe, and quetiapine. Last, we demonstrate that nIRHT can be introduced into the brain extracellular space in acute striatal brain slices and can be implemented to image exogenous 5-HT. While we have implemented SELEC to develop an optical probe for 5-HT here, the platform is fundamentally generic for generating other optical probes of neurological relevance.

RESULTS

SELEC enables high-throughput screening of single-stranded DNA–SWCNT constructs for 5-HT neuromodulator sensitivity

Previous work has demonstrated that semiconducting nIR fluorescent SWCNT, when noncovalently functionalized by amphiphilic polymers, such as single-stranded DNA (ssDNA), can generate synthetic molecular recognition elements on the SWCNT surface. The resulting ssDNA-SWCNT moiety can then selectively bind a molecular analyte for its optical detection (*22–25*). The process of generating ssDNA-SWCNT nanosensor candidates, and their screening against target analytes, has since revealed optical nanosensors for neurotransmitters including a $(GT)_6$-SWCNT nanosensor for dopamine (*24*), which was subsequently used to image dopamine dynamics in the brain striatum and capture the influence of dopamine receptor drugs on dopamine dynamics at the level of individual synapses (*26*). Despite the nascent utility of SWCNT-based nanosensor technology, the nanosensor screening process involves a heuristic approach in which each nanosensor candidate must be synthesized individually before screening, limiting candidate nanosensor libraries to a few dozen, thus restricting the throughput of nanosensor discovery. Here, we develop and validate an evolution-based approach for producing ssDNA-SWCNT nanosensors in which upward of 6.9×10^{10} unique ssDNA sequences are assessed for their ability to bind to a molecular analyte and produce an optical response. This strategy is inspired by SELEX protocols for aptamer generation (*27*) and entails systematic evolution of ssDNA ligands by exponential enrichment following adsorption to carbon nanotubes (SELEC), which we implement to identify ssDNA-SWCNT constructs that optically respond to neurotransmitter 5-HT. We designed our initial ssDNA library to be composed of 6.9×10^{10} random 18-mer ssDNA sequences flanked by two $(C)_6$-mers and two 18-mer primer regions for polymerase chain reaction (PCR) amplification (Fig. 1A). The 6-mer $(C)_6$ sequence was introduced because this was previously shown to have a high affinity for the SWCNT surface (*28*) and could thus serve as a SWCNT-binding spacer sequence to separate the random 18-mer sequence from the PCR primer sequences. This ssDNA library was used to suspend SWCNT using a previously described sonication protocol (*24*) to create a SWCNT suspension with 6.9×10^{10} unique ssDNA sequences for both an experimental and control ssDNA-SWCNT sample: Our experimental sample was generated in PBS solution by sonicating 10 μg SWCNT with 2.8 mg of ssDNA and 100 nmol of 5-HT. Our control sample was generated similarly but without 5-HT. The relative excess of ssDNA over SWCNT was implemented to encourage competitive complexation of ssDNA to SWCNT surfaces. Furthermore, the control sample served the role of identifying ssDNA sequences that are only strong SWCNT surface binders or subject to PCR biases (*29*) during library preparation. In this manner, both experimental and control libraries could be generated for competitive binding of ssDNAs, followed by the removal of unbound ssDNA sequences, and next desorption and deep sequencing of high-affinity ssDNA binders with an Illumina HiSeq 4000 (Fig. 1A). For both the experimental and control libraries, we found that a total of six consecutive rounds of competitive ssDNA SWCNT binding, desorption, recovery, and amplification of high-affinity ssDNA binders was sufficient to generate several promising 5-HT candidate nanosensors.

The 50 most numerous, thus the putatively highest-affinity, sequences in the sixth round of the experimental group were identified, and their corresponding frequencies in the total rounds were plotted in Fig. 1B (see tables S1 and S2 for sequences of the top 10 binders). We observed a clear enrichment in the 50 highest-affinity sequences following the sixth round of SELEC, in which each sequence has a mean frequency value of 19×10^{-6}. Conversely, those sequences have mean frequency values of 1.6×10^{-6} and 3.8×10^{-6}, respectively, in rounds 4 and 5 and negligible or zero frequency preceding round 4. Next, the identity of each nucleotide base was evaluated with respect to position within the top 200 ranked sequences in each library. The round 2 experimental library showed a near random distribution of nucleotides at each position, with sequence identities near the ~25% expected value at each position (Fig. 1C). Following six rounds of SELEC, base identity preference trends emerged in the experimental (Fig. 1D) and control (fig. S1) libraries. For instance, nucleotide A was preferred with a frequency of 86 and 65% in the experimental and control libraries at position 7, the first nucleotide following the 5′ $(C)_6$ spacer. The experimental library round 6 sequences showed 65% C and 62% T identities at positions 23 and 24, respectively, indicating a preference toward a 3′ CT terminus within the random region of the sequence. This preference was not observed in control library round 6, which instead showed enrichment of a GNG motif (fig. S1). Libraries were analyzed further by counting the incidences of nucleotide trimers with respect to position in the top 200 ranked sequences of each library. This analysis produced a trimer frequency table per nucleotide position for each control and experimental libraries. Classical multidimensional scaling (MDS) was performed on these frequency tables to evaluate the statistical difference between libraries. MDS reduces the dimensionality of library frequency tables into a two-dimensional (2D) projection, preserving the distances between trimer counts across libraries. A 2D MDS plot on first and second principal coordinates showed that the experimental and control libraries at round 2 could not be distinguished, but the divergence between the experimental and control libraries became considerable by round 6 (Fig. 1E). Round 6 divergence was driven, in part, by differences in abundance of repeating patterns such as AC and GT repeats. These differences were quantified by plotting counts of palindromic trimers such as ACA and CAC, and GTG and TGT in the top 200 ranking sequences with respect to position (fig. S2 and Fig. 1, F and G). The repeating AC motif was preferred in both experimental and control SELEC groups and predominately located near the 5′ end. The repeating GT motif showed the largest contrast of motif population between experimental and control groups, which was selectively enriched at the 3′ end of the control group and not in the experimental group. We also performed direct principal components analysis of the top 200 ranked sequences in each SELEC

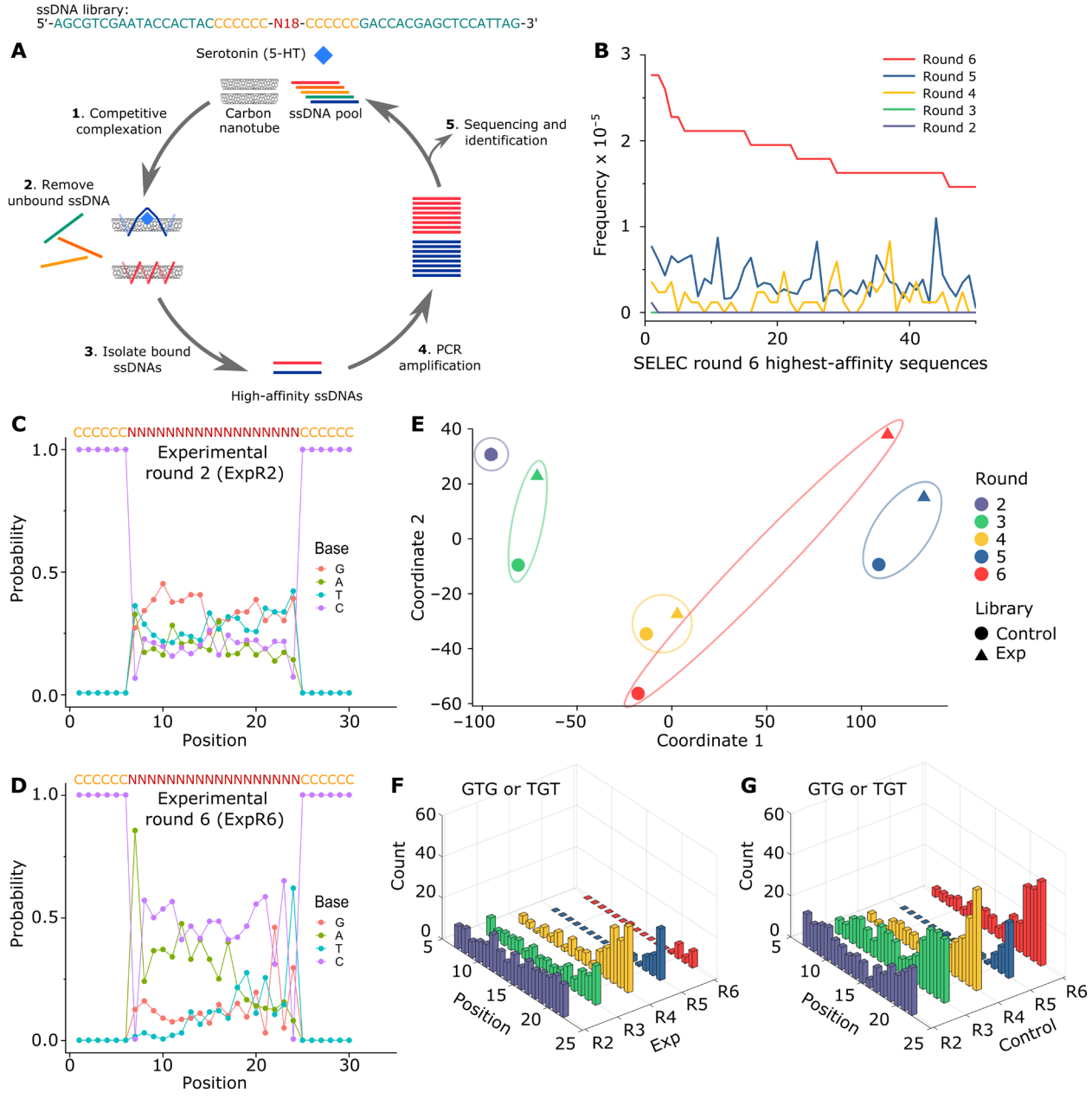

Fig. 1. SELEC evolves ssDNA-SWCNT nanosensors for 5-HT molecular recognition. (**A**) Schematic illustration of the SELEC evolution process. SWCNTs are mixed with a >10-fold mass excess of ssDNA with 100 μM 5-HT (experimental library) or alone (control library). (1) The mixture is sonicated to generate the ssDNA-SWCNT complex of either 5-HT–bound ssDNA-SWCNT (blue) or ssDNA-SWCNT (red). (2) Unbound ssDNAs are removed, and (3) bound ssDNAs are isolated from SWCNT by thermal desorption. (4) Isolated ssDNAs are amplified by PCR, and the ssDNA pool is prepared for the next selection round and (5) characterized by high-throughput sequencing. (**B**) Sequence frequency of the top 50 unique sequences in the sixth round of the experimental library, compared to their sequence prevalence in rounds 2 to 5. (**C** and **D**) Probability for each nucleotide at each position in the experimental library calculated from the top 200 sequences from (C) round 2 and (D) round 6. (**E**) MDS plot of trimer frequency table for the top 200 sequences in the experimental and control SELEC libraries at each round. Data are plotted on the first and second coordinates of MDS analysis. Contour lines are included for better visualization of mutual divergence between experimental and control SELEC libraries for the same round. Divergence at round 2 may be too small to be distinguished. (**F** and **G**) Palindromic trimer incidences of (GTG)/(TGT) at each nucleotide position for (F) experimental and (G) control libraries.

library. The first and second principal component axes do not distinguish between the experimental and control libraries in the first four rounds; however, divergence is observed in round 5, and distinct clustering of the experimental from control libraries can be observed by round 6 (fig. S3). Together, these results suggest that SELEC can evolve to select ssDNA sequences with high affinity for SWCNT in the presence and absence of an analyte and that the sequences evolved in each are nearly mutually exclusive, with only one common sequence in the top 1000 sequences of both libraries at round 6. We therefore hypothesize that the experimental library

will evolve ssDNA sequences that are selective for 5-HT when bound to SWCNT, whereas the control library will evolve ssDNA sequences that exhibit highest affinity for the SWCNT surface.

In vitro characterization of nIRHT optical nanosensor identified from SELEC evolution

We next analyzed the sensitivity of SELEC-evolved sequences to 5-HT when adsorbed to the surface of SWCNT. We denote sequences in experimental group as E**N**#**M** (**M**th place sequence of round **N** in the order of frequency) and sequences from the control group as C**N**#**M**. ssDNA-SWCNT nanosensor candidates were synthesized with the C_6 anchor domains, but without the primers used for PCR-based amplification. Omission of primer regions from testing ssDNA-SWCNT fluorescence responses was implemented to increase the mass density of the evolved N-18 library on the SWCNT surface. This omission was performed following confirmation that both **C_6-N18-C_6** and **primer-C_6-N18-C_6-primer** SELEC-evolved sequences from the experimental cohort showed enhanced sensitivity toward 5-HT, albeit with a reduced sensitivity for the latter, as predicted (fig. S4).

We prepared **C_6-N18-C_6** ssDNA-SWCNT constructs from the top 10 most abundant sequences from the experimental and control groups for SELEC rounds 3 to 6 and tested the $\Delta F/F_0$ fluorescence response of each ssDNA-SWCNT construct to addition of 100 μM 5-HT in phosphate-buffered saline (PBS) (figs. S5 and S6). $\Delta F/F_0$ is calculated as $(F - F_0)/F_0$ based on baseline fluorescence intensity before analyte addition (F_0) and fluorescence intensity 10 s after analyte addition (F) at 1195-nm emission. Multiple peaks in the fluorescence and absorption spectra of the nIRHT nanosensor showed the presence of different (n,m) SWCNT chiralities in ensemble mixture (Fig. 2C and fig. S7) (*30*), whereby the magnitude of the nIRHT nanosensor response to 5-HT is dependent on the (n,m) SWCNT chirality (fig. S8). Therefore, for consistency in nanosensor analysis, we use the optical response of the ~1195-nm nanosensor emission peak corresponding to the (8,6) SWCNT chirality, unless otherwise noted. As shown in Fig. 2A, we find that there is a statistically insignificant ($P = 0.055$) but qualitatively noticeable increase in ssDNA-SWCNT sensitivity for 5-HT at the final SELEC round, relative to the baseline fluorescence modulation of $\Delta F/F_0 = 0.73$ for the "unevolved" ssDNA-SWCNT sample prepared with the starting ssDNA library. Although the sensitivity difference is statistically insignificant ($P = 0.184$) between the experimental and control SELEC groups at round 6, enhanced sensitivity toward 5-HT is most evident for the experimental library in which highly 5-HT sensitive constructs ($\Delta F/F_0 > 1.2$) are only found in the experimental SELEC group and not in the control group (Fig. 2B). We identified the most 5-HT sensitive construct from both libraries and all SELEC rounds as E6#9 from the experimental library, which exhibited a $\Delta F/F_0$ of 1.94 ± 0.06 upon exposure to 100 μM 5-HT and could thus be used as a nIRHT nanosensor. We prepared E6#9 ssDNA-SWCNT with different mass ratios of ssDNA and SWCNT and found that the mass ratio does not affect the nanosensor response to 100 μM 5-HT (fig. S9). We observed the turn-on response of nIRHT to 5-HT to be nearly instantaneous followed by a low fluorescence decay with $\tau_{1/2} > 100$ s, which we confirmed is not a result of 5-HT structural or chemical change (figs. S10 and S11).

We next characterized nIRHT for use as a 5-HT brain imaging probe. We assessed the dynamic range of nIRHT to a 100 nM to 100 μM range of 5-HT concentrations and showed nIRHT sensitivity for 5-HT over a 100 nM to 50 μM dynamic range (Fig. 2D), largely suitable for measuring endogenous 5-HT dynamics, which are predicted to fall in the broad ~100 pM to ~1 μM concentration range (*31*–*35*). nIRHT showed a $\Delta F/F_0 = 0.20 \pm 0.03$ upon exposure to 1 μM 5-HT with a high signal-to-noise ratio of 12.4. Fitting nIRHT responsivity toward 5-HT to a Hill equation shows a micromolar dissociation constant (K_d) of 6.3 μM ($R^2 > 0.99$) for 5-HT (Fig. 2D), a K_d previously identified as optimal for imaging neuromodulation to balance nanosensor reversibility for capturing fast transients (*36*). We further confirmed that the ssDNA sequence for nIRHT has selective affinity for 5-HT through a solvatochromic shift assay with sodium cholate (SC) (fig. S12) and also confirmed that nIRHT shows a stable and reproducible fluorescence response to 5-HT for over a week after synthesis (figs. S13 and S14). We next compared the sensitivity of nIRHT to an ssDNA-SWCNT construct from the control SELEC group, C6#8, chosen for its strong affinity to the SWCNT surface (fig. S12). When bound to SWCNT, C6#8 showed reduced affinity ($K_d = 41$ μM) and a suppressed optical response ($\Delta F/F_0 = 0.53 \pm 0.01$ at 100 μM 5-HT) compared to nIRHT (Fig. 2D). These results suggest that SELEC can be implemented to evolve ssDNA-SWCNT selectivity for an analyte such as 5-HT and that nIRHT can serve as an optical reporter for 5-HT imaging.

Characterization of nIRHT as a nanosensor for 5-HT imaging in brain tissue

We next explored the utility of nIRHT for use as an optical probe to image extracellular 5-HT signaling in brain tissue. The response of nIRHT for 5-HT was assessed in aCSF, a common medium for imaging experiments in brain slice preparations. In aCSF, nIRHT demonstrated marginally superior performance than in PBS, with $\Delta F/F_0 = 2.45 \pm 0.07$ upon exposure to 100 μM 5-HT and $K_d = 10$ μM (Fig. 3A). We next examined the selectivity of nIRHT for 5-HT over other neurotransmitters. nIRHT nanosensor exhibited negligible $\Delta F/F_0$ response upon exposure to 100 μM acetylcholine, γ-aminobutyric acid, glutamate, tyrosine, and octopamine (Fig. 3B). Dopamine and norepinephrine, catecholamine neurotransmitters, induced a moderate response of $\Delta F/F_0 = 1.40 \pm 0.03$ and 1.06 ± 0.03 upon addition of 100 μM dopamine and norepinephrine, respectively. Notably, nIRHT exhibited a fivefold higher affinity for 5-HT over dopamine ($K_d = 6.3$ μM for 5-HT and $K_d = 33$ μM for dopamine) (fig. S15). We next measured nIRHT selectivity against 5-HT metabolites HTP, HIAA, and MTP, considering their high structural similarities to 5-HT. Addition of 100 μM HTP, HIAA, and MTP to nIRHT induced minimal fluorescence modulation of $\Delta F/F_0 = 0.02 \pm 0.02$, 0.17 ± 0.10, and -0.14 ± 0.03, respectively. We also studied the ability of nIRHT to measure 5-HT in the presence of interfering molecules. nIRHT preincubated with 100 μM dopamine, norepinephrine, or HIAA exhibited attenuated fluorescence response to 100 μM 5-HT with $\Delta F/F_0 = 0.09 \pm 0.01$, 0.12 ± 0.03, and 0.92 ± 0.12, respectively (fig. S16). Last, given the relevance of 5-HT receptor drugs on the study of 5-HT modulation and pharmacology, we assessed selectivity of nIRHT against non-selective agonists fluoxetine and MDMA, 5-HT_2 agonist 25I-NMOMe, and 5-HT_{1A} agonist quetiapine. Exposure of nIRHT to 100 μM fluoxetine, MDMA, 25I-NMOMe, and quetiapine induced negligible fluorescence modulation, and we additionally confirmed that 5-HT could be detected without attenuation even if nIRHT is preincubated with, and remains in the presence of, 1 μM of each of these drugs (Fig. 3C and fig. S17).

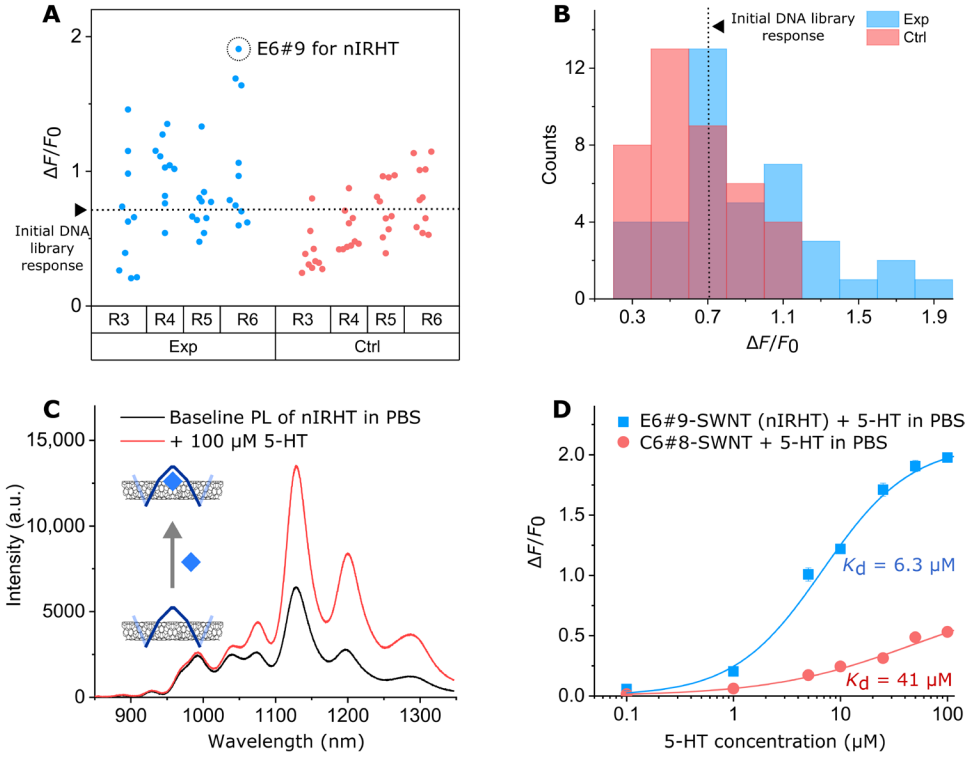

Fig. 2. Evolution of ssDNA-SWCNT demonstrates increased fluorescence sensitivity toward 5-HT. (**A**) $\Delta F/F_0$ upon addition of 100 μM 5-HT to top 10 ssDNA sequences from rounds 3 to 6 (R3 to R6) in experiment (Exp; blue circle) and control (Ctrl; red circle) SELEC groups ($n = 3$ trials). The most sensitive 5-HT nanosensor, E6#9, is indicated by a black dashed circle. $\Delta F/F_0$ from initial (round "zero") ssDNA-SWCNT library is represented by a dashed line. (**B**) Data from (A) are represented as a histogram. (**C**) Fluorescence spectra of E6#9 ssDNA-SWCNT before (black) and after (red) addition of 100 μM 5-HT. Inset: Schematic illustration of recognition of 5-HT by nIRHT nanosensor. a.u., arbitrary units. (**D**) $\Delta F/F_0$ 5-HT concentration dependence of E6#9-SWCNT (blue) and C6#8-SWCNT (red). Error bars denote SD from $n = 3$ independent trials and may be too small to be distinguished in the graph. Experimental data are fitted with the Hill equation (solid trace).

Toward endogenous 5-HT imaging, we next investigated the reversibility of the nIRHT nanosensor by immobilizing nIRHT in a microfluidic slide and imaging individual nIRHT nanosensors upon successive infusions of 100 μM 5-HT. nIRHT nanosensors were immobilized onto a 3-aminopropyltriethoxysilane (APTES)–treated glass slide and placed in a flow chamber with a syringe pump. The nanosensor chamber was exposed to three cycles of 100 μM 5-HT in PBS subsequently rinsed with PBS only, where the nIRHT nIR fluorescence response was imaged on an inverted microscope through 900-nm longpass filter to obtain nIR fluorescence from 900 to 1700 nm, as previously described (Fig. 3, D to F, and movie S1) (*26*). We observed nIRHT fluorescence increase and decrease as predicted by the influx and washing of 5-HT, respectively. Specifically, the time-dependent nIR fluorescence of three individual nanosensors was measured across three cycles and were found to be $\Delta F/F_0 = 1.55 \pm 0.01$, 1.71 ± 0.08, and 1.10 ± 0.14 (means ± SD for three cycles), which indicates that nIRHT nanosensors are reversible (Fig. 3G). We suggest that the variation in $\Delta F/F_0$ among nanosensors is a result of the chirality-dependent variability in SWCNT response as observed in bulk measurements. We further demonstrated that surface-immobilized SWCNT, without the ssDNA coating, do not respond to 5-HT, confirming the molecular recognition role of the ssDNA polymer when adsorbed to the SWCNT surface (fig. S18). Previous studies of ssDNA-SWCNT nanosensors have confirmed millisecond-scale nanosensor reversibility kinetics (*24*, *26*), the absence of photobleaching (*37*), and in vivo compatibility (*38*), suggesting that nIRHT could serve as an optical probe for long-term endogenous 5-HT imaging in the brain.

Last, we tested nIRHT nanosensor compatibility for 5-HT imaging in acute brain slices. Coronal mouse brain slices of 300 μm thickness were incubated with a nIRHT suspension (2 μg/ml) for 15 min and subsequently rinsed with aCSF to remove excess nIRHT. This labeling procedure was previously found to label acute slices with nanosensor localization in the brain extracellular space (*26*). nIRHT-labeled acute brain slices were coincubated with a cell-penetrating calcein-AM (acetoxymethyl) fluorescent dye to stain the live cell bodies, and we observed negligible colocalization (Pearson's correlation coefficient $R_p = -0.150$) between the fluorescence signal from calcein-AM and nIRHT (fig. S19), confirming that nIRHT nanosensors remain extracellular. We next imaged nIRHT-labeled slices in aCSF on a custom-built nIR fluorescence upright epifluorescence microscope equipped with a 900-nm longpass filter to obtain nIR fluorescence from 900 to 1700 nm (Fig. 3H). Time-dependent fluorescence images were recorded to confirm stable nIR fluorescence of nanosensors when no external stimuli were present (movie S2). We then investigated the ability of nIRHT nanosensors to respond to 5-HT in slice. Following acquisition of 1-min fluorescence baseline, bath application of 100 μM 5-HT resulted in a nIRHT fluorescence increase of $\Delta F/F_0 = 0.35 \pm 0.26$ (means ± SD) (Fig. 3, I and J, fig. S20, and movie S3). While nanosensor labeling in slice shows a heterogeneous distribution in the tissue, previous work has shown that nanosensor labeling density does not correlate with endogenous

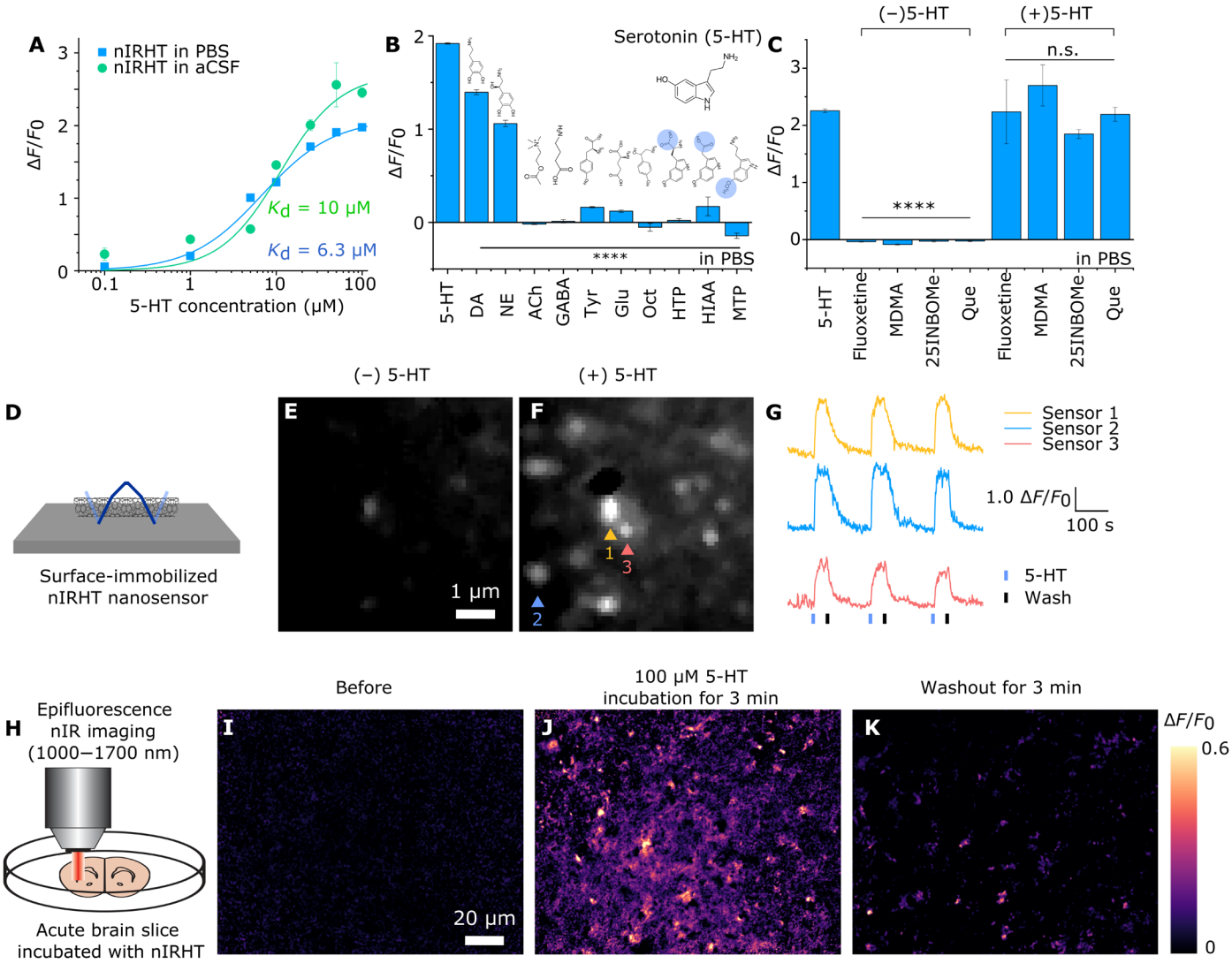

Fig. 3. Validation and use of nIRHT 5-HT nanosensors under neurologically relevant conditions. (**A**) 5-HT concentration–dependent $\Delta F/F_0$ of nIRHT nanosensor in PBS (blue squares) and aCSF (green circles) fit with the Hill equation (solid trace). (**B**) $\Delta F/F_0$ of nIRHT nanosensor upon exposure to 100 μM neurotransmitters and 5-HT metabolites [dopamine (DA), norepinephrine (NE), acetylcholine (ACh), γ-aminobutyric acid (GABA), tyrosine (Tyr), glutamate (Glu), and octopamine (Oct)]. Error bars are SD from $n = 3$ independent trials. (**C**) $\Delta F/F_0$ of nIRHT nanosensor upon exposure to 100 μM 5-HT with and without 1 μM 5-HT receptor drugs fluoxetine (nonselective agonist), 3,4-MDMA (nonselective agonist), 25I-NMOMe (5-HT_2 agonist), and quetiapine (Que) (5-HT_{1A} agonist). Error bars are SD from $n = 3$ independent trials. ****$P < 0.0001$. n.s., nonsignificant differences in one-way analysis of variance (ANOVA). (**D**) Reversibility of immobilized nIRHT nanosensors on glass substrate upon exposure to 100 μM 5-HT. (**E** and **F**) nIR fluorescence images of the same field of view (E) before and (F) after addition of 100 μM 5-HT. (**G**) $\Delta F/F_0$ of immobilized nanosensors upon exposure to 100 μM 5-HT (blue bar) and rinsed with PBS (black bar) in a flow chamber. (**H**) nIR imaging of dorsomedial striatum from mouse acute brain slice after nIRHT nanosensor loading into brain tissue. (**I** to **K**) $\Delta F/F_0$ images of the same field of view of an acute striatal brain slice (I) before, (J) 3 min after exogenous addition of 100 μM 5-HT, and (K) 3 min after rinsed with continuous aCSF flow. Bright $\Delta F/F_0$ hotspots following 5-HT bath application results from heterogeneous nIRHT slice labeling but does not correlate with endogenous neuromodulator responses observed in other studies (*26*).

neuromodulator $\Delta F/F_0$ response (*26*). Rinsing of the slice imaging chamber with aCSF confirmed that nIRHT fluorescence when in slice returns to baseline in the absence of 5-HT (Fig. 3K). Furthermore, sequential 5-HT perfusion and aCSF rinsing of the same nIRHT-labeled brain slice over the course of 1 hour generated consistent and reproducible nIRHT fluorescence response without noticeable attenuation of the nanosensor response (fig. S21). We further confirmed that nIRHT response to exogenous 5-HT can be observed for multiple biological replicates with modest variation ($\Delta F/F_0 = 0.35 \pm 0.26$ to 0.67 ± 0.14) in fluorescent response to addition of 100 μM 5-HT. We attribute the variability in nIRHT response across animals and brain slices to variable diffusive characteristics of 5-HT through the heterogeneous extracellular microstructures of brain tissue (fig. S22). As a control, an acute striatal brain slice labeled with a minimally 5-HT–responsive construct from our control library, C6#8-SWCNT, showed minimal $\Delta F/F_0 = 0.18 \pm 0.03$ (means ± SD fluorescence modulation in slice upon bath application of 100 μM 5-HT) (fig. S23). We also labeled an acute slice with SWCNT coated

with 1,2-distearoyl-*sn*-glycero-3-phosphoethanolamine-*N*-[amino-(polyethylene glycol)-2000] (DSPE-PEG-SWCNT), which has near-zero response upon exposure to 100 μM 5-HT, and this slice did not exhibit observable fluorescence response upon exogenous perfusion of 100 μM 5-HT (fig. S24). Last, we tested the robustness of the nIRHT nanosensor against endonuclease degradation by incubating nanosensor with S1 nuclease. We used the highest suggested concentration of endonuclease at 1000 U/ml, but note that nuclease concentrations in the brain extracellular space are unlikely to reach these levels. While free ssDNA degrades fully by 1 hour, ssDNA on SWCNT remains 78% intact at this time point (fig. S25), suggesting that surface adsorption promotes ssDNA biostability and motivates nIRHT use in tissue.

DISCUSSION

High spatiotemporal imaging of neuromodulatory signaling is essential to understand the dynamics of neuromodulator release and uptake in neural circuits and to elucidate the function of chemical neuromodulation in animal behavior (*39*). Synthetic probes are an attractive approach to imaging neuromodulators such as 5-HT owing to their photostability, compatibility with pharmacology, and feasibility for use in genetically intractable organisms. However, their generation depends either on trial-and-error screening for synthetic molecular recognition or conjugation of preexisting molecular recognition elements to nanomaterial signal transducers. Of note, the process of tethering the recognition moiety to a surface, particularly with nanomaterial signal transducers, often compromises the fidelity, specificity, and sensitivity of recognition elements due to surface steric effects, further limiting advances in synthetic optical probes. Here, we develop an approach to generate nIR optical probes through evolution of ssDNA-SWCNT selectivity toward 5-HT. ssDNA-SWCNT constructs whose polymer corona phase recognizes 5-HT were evolved from an initial 18-mer nucleotide library of $>10^{10}$ unique sequences by inducing competitive complexation between ssDNAs and SWCNTs in the presence of 5-HT through a process we termed SELEC. Previous studies have shown that analytes that induce selective fluorescence modulation of SWCNTs also stabilize the ssDNA corona (*24*); thus, we reason that evolved 5-HT recognizing sequences may preferentially populate the evolved ssDNA pool via stabilization of the 5-HT–ssDNA–SWCNT constructs. Conversely, the control SELEC library evolved in the absence of 5-HT should contain ssDNA sequences with high affinity for the SWCNT surface but not specifically for 5-HT. We find that pE6#9-SWCNT (the 5-HT–responsive nIRHT nanosensor with PCR primer regions) is stabilized by the presence of 5-HT substantially more so than pR0-SWCNT (the initial unevolved ssDNA library) (fig. S9). This result further indicates the ability of SELEC to evolve ssDNA-SWCNT nanosensors for selective recognition of analytes such as 5-HT. Together, these data demonstrate that SELEC can be implemented to rapidly screen large libraries of ssDNA-SWCNT constructs to evolve selectivity for small biomolecule analytes, circumventing low-throughput screening of these constructs previously used for SWCNT-based nanosensor development. It is feasible that SELEC could be implemented for other ssDNA-SWCNT technologies such as SWCNT-based chirality separation (*30*, *40*, *41*), which is strongly dependent on SWCNT surface adsorption of specific ssDNA sequences. Furthermore, because SELEC is fundamentally agnostic to the biomolecule analyte(s), SELEC may be implemented to develop nIR optical probes for other small-molecule targets of interest.

By implementing SELEC to evolve molecular recognition for neuromodulator 5-HT, we identified a nanosensor, nIRHT, with $\Delta F/F_0$ of 1.94 ± 0.06 in PBS and $\Delta F/F_0$ of up to 2.45 ± 0.07 in aCSF. Furthermore, we demonstrated that nIRHT provides a selective optical response for 5-HT against 5-HT metabolites, other neuromodulators, and pharmacology of relevance to 5-HT neuromodulation. While neurotransmitter dopamine also induced a moderate $\Delta F/F_0$ = 1.36 fluorescence increase of nIRHT (Fig. 3B), nIRHT exhibits a fivefold greater affinity for 5-HT over dopamine with $K_{d,5\text{-HT}}$ = 6.3 μM and $K_{d,dopamine}$ = 33 μM (fig. S11). In the future, implementing an additional "positive" selection library could help identify sequences with domains uniquely responsive to interfering molecules and eliminate those motifs from positive hits for the target ligand. It is noteworthy that the synthetically evolved nIRHT nanosensor shows negligible cross-responsivity with 5-HT precursors and metabolites and 5-HT receptor agonists and antagonists. Many optical probes for neurochemicals are based on proteins engineered from endogenous receptors and thus show cross-reactivity with receptor-targeting drugs. However, because the molecular recognition sites of nIRHT nanosensors are synthetic in nature, we demonstrate that nIRHT nanosensors do not show fluorescence modulation upon exposure to 5-HT receptor drugs fluoxetine, MDMA, 25I-NMOMe, and quetiapine (Fig. 3C). Thus, nIRHT optical probes and others of its class could enable insights into synaptic-level effects of 5-HT receptor agonists and antagonists to further our understanding of pharmacology of relevance to major depressive disorder (*6*), bipolar disorder (*7*), autism (*8*), schizophrenia (*9*), anxiety (*10*), and addiction (*11*), among others.

In comparison to the reported methodologies for 5-HT dynamic imaging such as FSCV (fast-scan cyclic voltammetry) (*13*), microdialysis (*14*), and paramagnetic 5-HT binding proteins for magnetic resonance imaging (*42*), nIRHT nanosensors are promising high spatiotemporal fluorescence imaging probes for studying 5-HT neuromodulation, which provide submicrometer spatial resolution, reversibility, photostability, and selectivity against 5-HT metabolites and receptor-targeting drugs. Furthermore, SWCNT fluoresce in a unique nIR window (1000 to 1300 nm), which reduces photon scattering and enhances imaging penetration depths, enabling through-cranium (*43*) and in vivo imaging (*38*). This optical window could enable the through-cranium fluorescence imaging of cortical 5-HT neuromodulation without a cranial window for chronic 5-HT imaging in animal models, although it is necessary to note that probe delivery may require cranial surgeries or injections similar to the status quo for delivery of adeno-associated viruses (*43*, *44*). Furthermore, previous work has demonstrated that SWCNT-based neuromodulator probes are tractable for use in nonmodel species (*26*), further expanding the repertoire of neurological studies to be undertaken with nIRHT and other probes of its class.

MATERIALS AND METHODS

Materials

HiPCo SWCNTs were purchased from NanoIntegris (batch #27-104). Serotonin hydrochloride (hydroxytryptamine hydrochloride), dopamine hydrochloride, acetylcholine, γ-aminobutyric acid (GABA), tyrosine, glutamate, octopamine, HTP, HIAA, MTP, fluoxetine, 3,4-MDMA, 25-NMOMe, and quetiapine were purchased from Sigma-Aldrich. All ssDNA sequences were purchased from Integrated DNA Technologies (IDT; USA).

Optical characterization of SWCNT

nIR fluorescence spectra were measured with a 20× objective on an inverted Zeiss microscope (Axio Observer.D1) coupled to a spectrograph (SCT 320, Princeton Instruments) and liquid nitrogen–cooled InGaAs linear array detector (PyLoN-IR, Princeton Instruments). A 721-nm laser (OptoEngine LLC) was used as the excitation light source for all spectroscopy and imaging studies. The absorption spectra were measured with a UV-3600 Plus absorption spectrophotometer (Shimadzu). Our custom nIR spectrometer and microscope have been described in detail in previous works (*45*, *46*).

SELEC experimental protocol

The initial ssDNA random library was purchased from IDT (USA), which consisted of 18 random nucleotides flanked by two fixed 6-mer $(C)_6$ and two 18-mer primer regions for PCR amplification: AGCGTCGAATACCACTAC-CCCCCC-N18-CCCCCC-GACCACGAGCTCCATTAG. For the first round, 100 nmol of the ssDNA library was dissolved in PBS buffer, and the mixture was denatured by heating at 95°C for 5 min and subsequently cooled to room temperature. For the experimental SELEC group to evolve 5-HT molecular recognition, the ssDNA library was incubated with 100 μM 5-HT for 10 min in 0.99 ml of PBS buffer. Next, 10 μg of SWCNT was added to the ssDNA and 5-HT mixture. A separate SELEC control group was prepared as described above but without the addition of 5-HT. The resulting mixtures were bath-sonicated for 2 min and next probe tip-sonicated (Cole-Parmer Ultrasonic Processor, 3-mm tip) for 10 min at 5-W power in an ice bath. After sonication, the black SWCNT suspension was centrifuged for 60 min at 16,100*g* to precipitate any unsuspended SWCNT, and the supernatant containing the ssDNA-SWCNT construct solution was collected. The supernatant was spin-filtered using a 100-kDa molecular weight cutoff (MWCO) centrifugal filter (Amicon Ultra-0.5, Millipore) at 6000 rpm for 5 min with deoxyribonuclease (DNase)–free water to remove unbound ssDNAs and 5-HT, and the remaining solution was collected. The spin filtration was repeated five times. Next, the purified ssDNA-SWCNT suspension was heated at 95°C for 1 hour to detach surface-bound ssDNAs from SWCNT. Following heating, black SWCNT aggregates were observed, as expected when the ssDNA corona desorbs from the SWCNT surface. The ssDNA solution with aggregated SWCNT was centrifuged for 10 min at 16,100*g* to further pellet undissolved SWCNT, and the supernatant containing ssDNA was collected. The collected ssDNA library was amplified by PCR using a FAM-modified forward primer (FAM-AGCGTCGAATACCACTAC) and biotinylated backward primer (biotin-CTAATGGAGCTCGTGGTC), following a previously described protocol (*27*). Standard solution conditions for PCR amplification were used as follows to maximize double-stranded DNA (dsDNA) yield while reducing by-products after amplification: 2.5 U of Hot Start Taq DNA polymerase (New England BioLabs), 1× Hot Start Taq reaction buffer, 1 μM forward primer, 1 μM backward primer, 500 μM deoxynucleotide triphosphate, and ssDNA library template (~100 ng/ml) in a total 10-ml volumes for each of the 100-μl volume 96-well reaction plates. A negative control well was prepared without ssDNA library template. A preparative PCR was performed with the following standard cycling conditions: initial denaturation for 150 s at 95°C, *N* cycles of denaturation for 30 s at 95°C and annealing for 30 s at 50°C and extension for 30 s at 72°C, and final extension for 180 s at 72°C. The cycle number *N* was determined before preparative PCR, which yielded maximal ssDNA and negligible PCR by-product formation (usually between 20 and 30 cycles). Next, 100 μl of the PCR products from each of the experimental and the control SELEC libraries was separately collected and purified with a GeneJET PCR Purification kit (Thermo Fisher Scientific) for preparation of high-throughput sequencing libraries. PCR products were confirmed by gel electrophoresis in a 4% agarose gel (low-range ultra agarose, Bio-Rad Laboratories) in 1× tris-borate-EDTA buffer (run for 18 min at 110 V). After electrophoresis, the gel was stained with SYBR Gold, and DNA bands were observed under ultraviolet light. To generate ssDNA from PCR products, 2.5 ml of streptavidin-coated beads (Streptavidin Sepharose High Performance, GE Healthcare) was placed on a sintered glass Buchner funnel (pore size, <10 μm) and washed with 10 ml of PBS buffer. The PCR product solution was incubated with the beads for 30 min and passed through the funnel. The incubation step was repeated three times to bind dsDNA onto the beads, and the beads were washed again with 10 ml of water. To elute the FAM-labeled ssDNAs, 8 ml of 0.2 M NaOH aqueous solution was added slowly to the beads, and the eluate was collected containing the FAM-labeled ssDNAs. The eluted solution was desalted with a NAP-10 desalting column (GE Healthcare) and concentrated using a DNA SpeedVac dryer. The amount of ssDNA was quantified by absorbance at 260 nm, and usually 2 to 5 nmol of ssDNA were obtained and used for the next round of SELEC. It usually takes 3 to 4 days to accomplish one round of SELEC. For the control SELEC library evolved with only ssDNA and SWCNT in the absence of 5-HT, the steps above were performed without 5-HT coincubation.

High-throughput sequencing and analysis

Sequencing libraries were prepared by using two sequential PCR steps (*47*) to add Illumina TruSeq universal adapter sequences and sequencing indices for multiplexed sequencing of rounds 2 to 6 from experimental and control SELEC groups. The sequencing libraries were sequenced with an Illumina HiSeq 4000 at the Genomic Sequencing Laboratory at the University of California, Berkeley, which generated about 20 million raw sequences from each round. We filtered out sequences that did not contain correct fixed regions (18-mer from 5′ primer + 6-mer cytosine block + 18-mer random region + 6-mer cytosine block + 3-mer from 3′ primer). A FASTAptamer toolkit was used to filter out and determine sequence frequencies (*48*). In the manuscript, all experiments used ssDNA sequences comprising only the 18-mer random region flanked by 6-mer cytosine blocks at each end (without PCR primer regions), unless otherwise noted. For classical MDS, the frequencies of trimers (e.g., ACA) at each position in the top 200 ranking sequences from the experimental or control SELEC libraries at each round were calculated and used as input parameters. 2D MDS analysis was performed by using the cmdscale() function of the stats package in R.

ssDNA-SWCNT construct preparation for nanosensor characterization

To characterize nanosensor properties such as fluorescence sensitivity and selectivity to 5-HT, ssDNA-functionalized SWCNT constructs were generated with the following protocol: 1 mg of HiPCo SWCNT was added to 0.9 ml of PBS buffer, and the solution was mixed with 100 μl of 1 mM ssDNA. The resulting mixture was bath-sonicated for 2 min and tip-sonicated for 10 min at 5-W power in an ice bath. After sonication, the black ssDNA-SWCNT suspension was centrifuged for 30 min at 16,100*g* to precipitate nondispersed SWCNT, and the supernatant containing solubilized ssDNA-SWCNT was

collected. The supernatant was spin-filtered with 100-kDa MWCO centrifugal filters at 6000 rpm for 5 min with DNase-free water to remove unbound ssDNAs, and the purified solution at the top of the filter was collected. This spin filtration to remove unbound ssDNA was repeated three times. The ssDNA-SWCNT suspension was diluted with PBS buffer and stored at 4°C until use. The concentration of the ssDNA-SWCNT suspension was calculated by measuring its absorbance at 632 nm with an extinction coefficient for SWCNT (*25*) of 0.036 $(mg/liter)^{-1}$ cm^{-1}.

Spectral solvatochromic shift of ssDNA-SWCNT induced by SC

For SC-induced spectral shift assays without 5-HT, ssDNA-SWCNT samples were prepared by creating a 100-µl PBS solution with ssDNA-SWCNT (20 mg/liter) generated with the following ssDNAs: pR0, pE6#9, and pC6#8 containing the PCR primer regions (table S3). These solutions were loaded onto a custom-built nIR fluorescence spectrometer, and the time-dependent nIR fluorescence spectra were measured before and after the addition of 100 µl of 0.5 weight % (wt %) SC in PBS. The spectral blueshift was observed for all the fluorescence peaks, and we quantified the time-dependent spectral shift of the (8,6) SWCNT chirality peak (~1195 nm). For the SC-induced spectral shift assay with 5-HT preincubation, a 100-µl PBS solution containing ssDNA-SWCNT (20 mg/liter) of the abovementioned sequences was incubated with 100 µM 5-HT for 1 min. The fluorescence spectra of the ssDNA-SWCNT constructs were subsequently measured every 2 s for a total of ~6 min, with 0.5 wt % SC added to each sample at a time point marked by a solid black arrow (fig. S9).

Screening the fluorescence response of ssDNA-SWCNT constructs to 5-HT and other analytes

Fluorescence spectra of 198-µl ssDNA-SWCNT suspensions (10 mg/liter) in PBS were measured before and 10 s after the addition of 2 µl of 10 mM 5-HT solution for a final 5-HT concentration of 100 µM. We analyzed the nIR fluorescence change of the (8,6) SWCNT chirality peak (~1195 nm) in this study. $\Delta F/F_0$ was calculated as $\Delta F/F_0 = (F - F_0)/F_0$ based on the baseline fluorescence intensity before analyte addition F_0 and the fluorescence intensity 10 s after analyte addition for the (8,6) SWCNT chirality (~1195 nm), F. Most of the analyte solutions were prepared with dissolution in deionized (DI) water as 10 mM concentration stocks, except tyrosine, which was dissolved in dimethyl sulfoxide. Serotonin hydrochloride and dopamine hydrochloride were used to prepare the analyte solutions to prevent oxidation of the neuromodulators under ambient conditions, and the hydrochloride salt did not affect the pH of resulting mixture because the PBS buffer capacity (~10 mM) was substantially higher than the amount of hydrochloride in the neuromodulator stocks (0.1 mM). All $\Delta F/F_0$ measurements were performed in triplicate, and the mean and SD of triplicate measurements were plotted. The assessment of 5-HT metabolites on nIRHT fluorescence was tested by preparing a 198-µl nIRHT suspension (10 mg/liter) in PBS and taking the nIR fluorescence spectra before and 10 s after the addition of 2 µl of 10 mM 5-HT metabolites (HTP, HIAA, and MTP). The assessment of 5-HT receptor drugs on nIRHT fluorescence was tested by preincubating a 198-µl nIRHT suspension (10 mg/liter) in 1 µM drug (fluoxetine, MDMA, 25I-NMOMe, and quetiapine) in PBS and taking the nIR fluorescence spectra before and after the addition of 2 µl of 10 mM 5-HT. All concentration-dependent $\Delta F/F_0$ response curves were fitted to the Hill equation (*23*) to determine K_d's.

To measure the optical $\Delta F/F_0$ response of nIRHT in brain-relevant environments, we prepared a nIRHT stock solution (10 mg/liter) in aCSF composed of 119 mM NaCl, 26.2 mM $NaHCO_3$, 2.5 mM KCl, 1 mM NaH_2PO_4, 1.3 mM $MgCl_2$, 10 mM glucose, and 2 mM $CaCl_2$ (pH 7.4). In a separate assay, 100 µl of nIRHTs (100 mg/l) was incubated in 900 µl of stock human cerebrospinal fluid (from Lee Biosolutions).

NMR analysis of 5-HT after coincubation with nIRHT

For nuclear magnetic resonance (NMR) analysis, PBS buffer was prepared in D_2O (PBS-d). nIRHT (396 µl; 10 mg/liter) in PBS-d was mixed with 4 µl of 10 mM 5-HT in D_2O. The mixture was excited with a 721-nm laser for 10 min on the same nIR fluorescence spectrometer used for nanosensor screening and fluorescence measurements. The solution was spin-filtered using a 100-kDa MWCO centrifugal filter at 6000 rpm for 5 min with D_2O, and the flow-through solution was collected. The ^1H NMR spectra of the flow-through solution were measured with a 400-MHz Avance AVB-400 NMR (Bruker). The ^1H NMR spectra of a 0.1 mM 5-HT solution without laser excitation in D_2O were also measured as a control.

Reversibility of nIRHT nanosensors immobilized in a microfluidic chamber

A glass coverslip (#1.5; thickness, 0.17 mm; HS159879H, Heathrow Scientific) was functionalized with APTES (Sigma-Aldrich) by soaking in 10% (v/v) APTES in anhydrous ethanol for 5 min, following a previously reported protocol (*26*). The coverslip was then rinsed with DI water and left to dry. The coverslip was then fixed onto an ibidi µ-Slide $VI^{0.5}$ forming six microfluidic channels. Next, 100 µl of PBS was pipetted through a microfluidic channel. The channel was then filled with 50 µl of a nIRHT solution (10 mg/liter) and left to incubate at room temperature for 5 min. The channel was rinsed using three successive washes of 50-µl PBS. The surface-immobilized nIRHT in PBS was then imaged on an inverted light microscope with 721-nm excitation and a Ninox VIS-SWIR 640 camera (Raptor Photonics). Fluorescence signal was collected through a 900-nm longpass filter. One end of the flow channel was connected to a syringe pump (Harvard Apparatus) with Luer lock fittings. Before the start of image acquisition, the opposite flow reservoir was filled with PBS, and the pump was set to refill mode at a volumetric flow rate of 100 µl/min. Once the liquid in the reservoir was depleted, 50 µl of 100 µM 5-HT in PBS was added. The process was repeated using alternating additions of 200 µl of PBS and 50 µl of 5-HT solution.

To test the optical response of bare SWCNT immobilized onto a glass substrate, an SDS-coated SWCNT suspension was prepared: 1 mg of HiPCo SWCNT was added to 1 ml of 2 wt % SDS in PBS buffer. The resulting mixture was bath-sonicated for 2 min and tip-sonicated for 30 min at 5-W power in an ice bath. After sonication, the black suspension was centrifuged for 60 min at 16,100*g* to precipitate undissolved SWCNT, and the supernatant solution was collected. Fifty microliters of SDS-SWCNT (5 mg/liter) was incubated in a microfluidic slide as described above, and the SDS coating was gradually removed by introducing a continuous flow of PBS buffer into the channel for 1 hour at a flow rate of 50 µl/min. Following this surfactant stripping step, 50 µl of 10 µM 5-HT in PBS was added to the microfluidic channel.

nIRHT nanosensor imaging in an acute brain slice

Sixty-day-old C57Bl/6 strain mice were used for nIRHT brain slice imaging experiments. Mice were group-housed after weaning at P21

and kept with nesting material on a 12:12 light/dark cycle. All animal procedures were approved by the University of California Berkeley Animal Care and Use Committee. Acute brain slices were prepared using established protocols (*49*). Briefly, mice were deeply anesthetized via intraperitoneal injection of ketamine/xylazine cocktail, and transcardial perfusion was subsequently performed using ice-cold cutting buffer (119 mM NaCl, 26.2 mM $NaHCO_3$, 2.5 mM KCl, 1 mM NaH_2PO_4, 3.5 mM $MgCl_2$, 10 mM glucose, and 0 mM $CaCl_2$), after which the brain was rapidly extracted. The cerebellum and other connective tissues were trimmed using a razor blade, and the brain was mounted onto the cutting stage of a vibratome (Leica VT1200 S). Coronal slices (300 μm thick) including the dorsal striatum were prepared. Slices were incubated at 37°C for 60 min in oxygen-saturated aCSF (119 mM NaCl, 26.2 mM $NaHCO_3$, 2.5 mM KCl, 1 mM NaH_2PO_4, 1.3 mM $MgCl_2$, 10 mM glucose, and 2 mM $CaCl_2$) before use. Slices were then transferred to room temperature for 30 min before starting imaging experiments and were maintained at room temperature for the remainder of experimentation. For nanosensor labeling, slices were transferred into a small-volume brain slice incubation chamber (Scientific Systems Design Inc., AutoMate Scientific) and kept under oxygen-saturated aCSF (total of 5-ml volume). One hundred microliters of nIRHT nanosensor (100 mg/liter) was added to the 5-ml volume, and the slice was incubated in this solution for 15 min. The slice was subsequently recovered and rinsed in oxygen-saturated aCSF to wash off nIRHT that did not localize into the brain tissue. The rinsing step was performed by transferring the slice through three wells of aCSF in a 24-well plate (5 s in each well), followed by labeled slice transfer to the recording chamber with aCSF perfusion for a 15-min equilibration period before starting the imaging experimentation. All imaging experiments were performed at 32°C with continuous perfusion of oxygen-saturated aCSF to maintain brain slice viability. Ex vivo slice imaging was performed with a modified upright epifluorescence microscope mounted onto a motorized stage as we previously described (*26*). The brain slice labeled with nIRHT was illuminated with 785-nm light, and the fluorescence images were taken in a field of view within the brain dorsomedial striatum with an InGaAs array detector (Ninox 640, Raptor Photonics) with 100-ms exposure and a 60× objective. Fluorescence signal was collected through a 900-nm longpass filter. To observe nIRHT response to 5-HT influx, the brain slice was immersed in 3 ml of oxygen-saturated aCSF in the flow chamber, and 0.3 ml of 1 mM 5-HT in aCSF was added into the system without further mixing. After the fluorescence reached a plateau, the 5-HT in the chamber solution was slowly depleted by continuous flow of oxygen-saturated aCSF (washing). Time-dependent $\Delta F/F_0$ was calculated from multiple regions of interest identified by a custom image analysis program (available for download at https://github.com/jtdbod/Nanosensor-Brain-Imaging).

SUPPLEMENTARY MATERIALS

Supplementary material for this article is available at http://advances.sciencemag.org/cgi/content/full/5/12/eaay3771/DC1

Table S1. Ten most frequent ssDNA sequences from rounds 3 to 6 in experimental SELEC groups (E3 to E6).

Table S2. Ten most frequent ssDNA sequences from rounds 3 to 6 in control SELEC groups (C3 to C6).

Table S3. ssDNA sequences used in experiments: pR0 is the unevolved initial ssDNA library, pE6#9 and pC6#8 are sequences used for investigating the effect of the PCR primer region to the ssDNA-SWCNT 5-HT response and solvatochromatic shift assay by SC, and R0 is the PCR primer–truncated initial ssDNA library.

Fig. S1. Evolution of nucleotide identity prevalence in the control SELEC library.

Fig. S2. Prevalence of palindromic sequences evolved in SELEC experimental and control libraries.

Fig. S3. Scatter plots of principal component 1 versus principal component 2 for experimental and control SELEC library sequences.

Fig. S4. Truncation of primer region from ssDNA sequence improves the 5-HT response of ssDNA-SWCNT.

Fig. S5. ssDNA-SWCNT response to 5-HT from experimental and control SELEC groups.

Fig. S6. Raw fluorescence spectra of evolved ssDNA-SWCNT constructs.

Fig. S7. Absorption spectrum of nIRHT in DI water.

Fig. S8. Deconvolution of nIRHT fluorescence spectrum.

Fig. S9. The mass proportion of ssDNA and SWCNT for nIRHT synthesis does not affect nanosensor response upon exposure to 100 μM 5-HT.

Fig. S10. Time-dependent nIR fluorescence response of nIRHT nanosensor to various neurotransmitter and metabolite molecules.

Fig. S11. Fluorescence intensity profile of nIRHT nanosensors following 5-HT addition is not due to 5-HT oxidation.

Fig. S12. Solvatochromic spectral shift indicates that SELEC for 5-HT nanosensors selects for ssDNA sequences that have molecular recognition for 5-HT when adsorbed to SWCNT.

Fig. S13. Reproducibility of nIRHT nanosensor fluorescence response to 5-HT over time.

Fig. S14. nIRHT nanosensor performance reproducibility.

Fig. S15. $\Delta F/F_0$ dopamine concentration dependence of nIRHT in PBS.

Fig. S16. nIRHT nanosensor response in the presence of interfering agents.

Fig. S17. $\Delta F/F_0$ 5-HT concentration dependence of nIRHT preincubated with 1 μM fluoxetine in PBS.

Fig. S18. Null 5-HT fluorescence response of bare SWCNT.

Fig. S19. Visible and nIR widefield microscopy of the same region of an acute brain slice incubated with a cell-penetrating green fluorescent dye (calcein-AM) and nIR fluorescent nIRHT.

Fig. S20. Time-dependent nIRHT nanosensor response to exogenous 5-HT in acute mouse brain slice.

Fig. S21. $\Delta F/F_0$ response of a nIRHT-labeled acute slice upon repeat exposure to 100 μM 5-HT.

Fig. S22. Reproducibility of nIRHT-labeled acute brain slice imaging.

Fig. S23. $\Delta F/F_0$ response of a C6#8 ssDNA-SWCNT–labeled acute slice upon exposure to 100 μM 5-HT.

Fig. S24. $\Delta F/F_0$ response of a DSPE-PEG–coated SWCNT-labeled acute slice upon exposure to 100 μM 5-HT.

Fig. S25. Stability of nIRHT nanosensors against endonuclease degradation.

Fig. S26. nIRHT nanosensor response when preincubated with cerebrospinal fluid.

Movie S1. Time-dependent 5-HT–induced response of nIRHT in microfluidic chamber.

Movie S2. nIRHT-labeled brain dorsomedial striatum slice without external stimuli.

Movie S3. nIRHT-labeled brain dorsomedial striatum slice after addition of 100 μM 5-HT and subsequent washing by aCSF.

References (*50*–*60*)

View/request a protocol for this paper from *Bio-protocol*.

REFERENCES AND NOTES

1. M. Vaswani, F. K. Linda, S. Ramesh, Role of selective serotonin reuptake inhibitors in psychiatric disorders: A comprehensive review. *Prog. Neuropsychopharmacol. Biol. Psychiatry* **27**, 85–102 (2003).
2. S. P. Fernandez, A. Muzerelle, S. Scotto-Lomassese, J. Barik, A. Gruart, J. M. Delgado-García, P. Gaspar, Constitutive and acquired serotonin deficiency alters memory and hippocampal synaptic plasticity. *Neuropsychopharmacology* **42**, 512–523 (2016).
3. A. Barre, C. Berthoux, D. De Bundel, E. Valjent, J. Bockaert, P. Marin, C. Bécamel, Presynaptic serotonin 2A receptors modulate thalamocortical plasticity and associative learning. *Proc. Natl. Acad. Sci. U.S.A.* **113**, E1382–E1391 (2016).
4. P. J. Cowen, M. Browning, What has serotonin to do with depression? *World Psychiatry* **14**, 158–160 (2015).
5. M. Berger, J. A. Gray, B. L. Roth, The expanded biology of serotonin. *Annu. Rev. Med.* **60**, 355–366 (2009).
6. S. Nikolaus, H. Hautzel, A. Heinzel, H.-W. Müller, Key players in major and bipolar depression—A retrospective analysis of in vivo imaging studies. *Behav. Brain Res.* **232**, 358–390 (2012).
7. G. M. Sullivan, R. T. Ogden, M. A. Oquendo, J. S. D. Kumar, N. Simpson, Y.-y. Huang, J. J. Mann, R. V. Parsey, Positron emission tomography quantification of serotonin-1A receptor binding in medication-free bipolar depression. *Biol. Psychiatry* **66**, 223–230 (2009).
8. D. Adamsen, V. Ramaekers, H. T. B. Ho, C. Britschgi, V. Rüfenacht, D. Meili, E. Bobrowski, P. Philippe, C. Nava, L. Van Maldergem, R. Bruggmann, S. Walitza, J. Wang, E. Grünblatt, B. Thöny, Autism spectrum disorder associated with low serotonin in CSF and mutations in the *SLC29A4* plasma membrane monoamine transporter (PMAT) gene. *Mol. Autism* **5**, 43 (2014).

9. H. Y. Meltzer, Z. Li, Y. Kaneda, J. Ichikawa, Serotonin receptors: Their key role in drugs to treat schizophrenia. *Prog. Neuropsychopharmacol. Biol. Psychiatry* **27**, 1159–1172 (2003).
10. C. Gross, X. Zhuang, K. Stark, S. Ramboz, R. Oosting, L. Kirby, L. Santarelli, S. Beck, R. Hen, Serotonin$_{1A}$ receptor acts during development to establish normal anxiety-like behaviour in the adult. *Nature* **416**, 396–400 (2002).
11. C. P. Müller, J. R. Homberg, The role of serotonin in drug use and addiction. *Behav. Brain Res.* **277**, 146–192 (2015).
12. J. D. Clements, R. A. Lester, G. Tong, C. E. Jahr, G. L. Westbrook, The time course of glutamate in the synaptic cleft. *Science* **258**, 1498–1501 (1992).
13. C. John, S. Jones, Fast scan cyclic voltammetry of dopamine and serotonin in mouse brain slices, in *Electrochemical Methods for Neuroscience*, A. Michael, L. Borland, Eds. (CRC Press, 2007).
14. R. W. Fuller, Uptake inhibitors increase extracellular serotonin concentration measured by brain microdialysis. *Life Sci.* **55**, 163–167 (1994).
15. N. Nakatsuka, K.-A. Yang, J. M. Abendroth, K. M. Cheung, X. Xu, H. Yang, C. Zhao, B. Zhu, Y. S. Rim, Y. Yang, P. S. Weiss, M. N. Stojanović, A. M. Andrews, Aptamer–field-effect transistors overcome Debye length limitations for small-molecule sensing. *Science* **362**, 319–324 (2018).
16. P. Wang, M. Xia, O. Liang, K. Sun, A. F. Cipriano, T. Schroeder, H. Liu, Y.-H. Xie, Label-free SERS selective detection of dopamine and serotonin using graphene-Au nanopyramid heterostructure. *Anal. Chem.* **87**, 10255–10261 (2015).
17. K. S. Hettie, T. E. Glass, Turn-on near-infrared fluorescent sensor for selectively imaging serotonin. *ACS Chem. Neurosci.* **7**, 21–25 (2016).
18. A. Henke, Y. Kovalyova, M. Dunn, D. Dreier, N. G. Gubernator, I. Dincheva, C. Hwu, P. Šebej, M. S. Ansorge, D. Sulzer, D. Sames, Toward serotonin fluorescent false neurotransmitters: Development of fluorescent dual serotonin and vesicular monoamine transporter substrates for visualizing serotonin neurons. *ACS Chem. Neurosci.* **9**, 925–934 (2018).
19. S. Maiti, J. B. Shear, R. M. Williams, W. R. Zipfel, W. W. Webb, Measuring serotonin distribution in live cells with three-photon excitation. *Science* **275**, 530–532 (1997).
20. L. A. Colgan, I. Putzier, E. S. Levitan, Activity-dependent vesicular monoamine transporter-mediated depletion of the nucleus supports somatic release by serotonin neurons. *J. Neurosci.* **29**, 15878–15887 (2009).
21. S. K. Kaushalya, R. Desai, S. Arumugam, H. Ghosh, J. Balaji, S. Maiti, Three-photon microscopy shows that somatic release can be a quantitatively significant component of serotonergic neurotransmission in the mammalian brain. *J. Neurosci. Res.* **86**, 3469–3480 (2008).
22. G. Bisker, J. Dong, H. D. Park, N. M. Iverson, J. Ahn, J. T. Nelson, M. P. Landry, S. Kruss, M. S. Strano, Protein-targeted corona phase molecular recognition. *Nat. Commun.* **7**, 10241 (2016).
23. S. Kruss, M. P. Landry, E. V. Ende, B. M. A. Lima, N. F. Reuel, J. Zhang, J. Nelson, B. Mu, A. Hilmer, M. Strano, Neurotransmitter detection using corona phase molecular recognition on fluorescent single-walled carbon nanotube sensors. *J. Am. Chem. Soc.* **136**, 713–724 (2014).
24. A. G. Beyene, A. A. Alizadehmojarad, G. Dorlhiac, N. Goh, A. M. Streets, P. Král, L. Vuković, M. P. Landry, Ultralarge modulation of fluorescence by neuromodulators in carbon nanotubes functionalized with self-assembled oligonucleotide rings. *Nano Lett.* **18**, 6995–7003 (2018).
25. J. Zhang, M. P. Landry, P. W. Barone, J.-H. Kim, S. Lin, Z. W. Ulissi, D. Lin, B. Mu, A. A. Boghossian, A. J. Hilmer, A. Rwei, A. C. Hinckley, S. Kruss, M. A. Shandell, N. Nair, S. Blake, F. Sen, S. Sen, R. G. Croy, D. Li, K. Yum, J.-H. Ahn, H. Jin, D. A. Heller, J. M. Essigmann, D. Blankschtein, M. S. Strano, Molecular recognition using corona phase complexes made of synthetic polymers adsorbed on carbon nanotubes. *Nat. Nanotechnol.* **8**, 959–968 (2013).
26. A. G. Beyene, K. Delevich, J. T. Del Bonis-O'Donnell, D. J. Piekarski, W. C. Lin, A. W. Thomas, S. J. Yang, P. Kosillo, D. Yang, G. S. Prounis, L. Wilbrecht, M. P. Landry, Imaging striatal dopamine release using a non-genetically encoded near-infrared fluorescent catecholamine nanosensor. *Sci. Adv.* **5**, eaaw3108 (2019).
27. K. Sefah, D. Shangguan, X. Xiong, M. B. O'Donoghue, W. Tan, Development of DNA aptamers using Cell-SELEX. *Nat. Protocols* **5**, 1169–1185 (2010).
28. M. P. Landry, L. Vuković, S. Kruss, G. Bisker, A. M. Landry, S. Islam, R. Jain, K. Schulten, M. S. Strano, Comparative dynamics and sequence dependence of DNA and RNA binding to single walled carbon nanotubes. *J. Phys. Chem. C* **119**, 10048–10058 (2015).
29. S. G. Acinas, R. Sarma-Rupavtarm, V. Klepac-Ceraj, M. F. Polz, PCR-induced sequence artifacts and bias: Insights from comparison of two 16S rRNA clone libraries constructed from the same sample. *Appl. Environ. Microbiol.* **71**, 8966–8969 (2005).
30. X. Tu, S. Manohar, A. Jagota, M. Zheng, DNA sequence motifs for structure-specific recognition and separation of carbon nanotubes. *Nature* **460**, 250–253 (2009).
31. H. Yang, A. B. Thompson, B. J. McIntosh, S. C. Altieri, A. M. Andrews, Physiologically relevant changes in serotonin resolved by fast microdialysis. *ACS Chem. Neurosci.* **4**, 790–798 (2013).
32. F. Crespi, K. F. Martin, C. A. Marsden, Measurement of extracellular basal levels of serotonin in vivo using nafion-coated carbon fibre electrodes combined with differential pulse voltammetry. *Neuroscience* **27**, 885–896 (1988).
33. A. Abdalla, C. W. Atcherley, P. Pathirathna, S. Samaranayake, B. Qiang, E. Peña, S. L. Morgan, M. L. Heien, P. Hashemi, In vivo ambient serotonin measurements at carbon-fiber microelectrodes. *Anal. Chem.* **89**, 9703–9711 (2017).
34. C. J. Griessenauer, S.-Y. Chang, S. J. Tye, C. J. Kimble, K. E. Bennet, P. A. Garris, K. H. Lee, Wireless Instantaneous Neurotransmitter Concentration System: Electrochemical monitoring of serotonin using fast-scan cyclic voltammetry—A proof-of-principle study. *J. Neurosurg.* **113**, 656–665 (2010).
35. H. Yang, M. M. Sampson, D. Senturk, A. M. Andrews, Sex- and SERT-mediated differences in stimulated serotonin revealed by fast microdialysis. *ACS Chem. Neurosci.* **6**, 1487–1501 (2015).
36. A. G. Beyene, I. R. McFarlane, R. L. Pinals, M. P. Landry, Stochastic simulation of dopamine neuromodulation for implementation of fluorescent neurochemical probes in the striatal extracellular space. *ACS Chem. Neurosci.* **8**, 2275–2289 (2017).
37. A. A. Boghossian, J. Zhang, P. W. Barone, N. F. Reuel, J.-H. Kim, D. A. Heller, J.-H. Ahn, A. J. Hilmer, A. Rwei, J. R. Arkalgud, C. T. Zhang, M. S. Strano, Near-infrared fluorescent sensors based on single-walled carbon nanotubes for life sciences applications. *ChemSusChem* **4**, 848–863 (2011).
38. T. V. Galassi, P. V. Jena, J. Shah, G. Ao, E. Molitor, Y. Bram, A. Frankel, J. Park, J. Jessurun, D. S. Ory, A. Haimovitz-Friedman, D. Roxbury, J. Mittal, M. Zheng, R. E. Schwartz, D. A. Heller, An optical nanoreporter of endolysosomal lipid accumulation reveals enduring effects of diet on hepatic macrophages in vivo. *Sci. Transl. Med.* **10**, eaar2680 (2018).
39. M. Ludwig, D. Apps, J. Menzies, J. C. Patel, M. E. Rice, Dendritic release of neurotransmitters. *Compr. Physiol.* **7**, 235–252 (2016).
40. Y. Yang, M. Zheng, A. Jagota, Learning to predict single-wall carbon nanotube-recognition DNA sequences. *NPJ Comput. Mater.* **5**, 3 (2019).
41. J. A. Fagan, C. Y. Khripin, C. A. Silvera Batista, J. R. Simpson, E. H. Hároz, A. R. Hight Walker, M. Zheng, Isolation of specific small-diameter single-wall carbon nanotube species via aqueous two-phase extraction. *Adv. Mater.* **26**, 2800–2804 (2014).
42. A. Hai, L. X. Cai, T. Lee, V. S. Lelyveld, A. Jasanoff, Molecular fMRI of serotonin transport. *Neuron* **92**, 754–765 (2016).
43. G. Hong, S. Diao, J. Chang, A. L. Antaris, C. Chen, B. Zhang, S. Zhao, D. N. Atochin, P. L. Huang, K. I. Andreasson, C. J. Kuo, H. Dai, Through-skull fluorescence imaging of the brain in a new near-infrared window. *Nat. Photonics* **8**, 723–730 (2014).
44. A. K. Patlolla, P. K. Patra, M. Flountan, P. B. Tchounwou, Cytogenetic evaluation of functionalized single-walled carbon nanotube in mice bone marrow cells. *Environ. Toxicol.* **31**, 1091–1102 (2016).
45. L. Chio, D. Yang, M. Landry, Surface engineering of nanoparticles to create synthetic antibodies, in *Synthetic Antibodies: Methods and Protocols*, T. Tiller, Ed. (Springer, 2017), pp. 363–380.
46. A. G. Beyene, G. S. Demirer, M. P. Landry, Nanoparticle-templated molecular recognition platforms for detection of biological analytes. *Curr. Protoc. Chem. Biol.* **8**, 197–223 (2016).
47. M. A. Ditzler, M. J. Lange, D. Bose, C. A. Bottoms, K. F. Virkler, A. W. Sawyer, A. S. Whatley, W. Spollen, S. A. Givan, D. H. Burke, High-throughput sequence analysis reveals structural diversity and improved potency among RNA inhibitors of HIV reverse transcriptase. *Nucleic Acids Res.* **41**, 1873–1884 (2013).
48. K. K. Alam, J. L. Chang, D. H. Burke, FASTAptamer: A bioinformatic toolkit for high-throughput sequence analysis of combinatorial selections. *Mol. Ther. Nucleic Acids* **4**, e230 (2015).
49. D. J. Piekarski, J. R. Boivin, L. Wilbrecht, Ovarian hormones organize the maturation of inhibitory neurotransmission in the frontal cortex at puberty onset in female mice. *Curr. Biol.* **27**, 1735–1745.e3 (2017).
50. N. Nakatsuka, M. M. Hasani-Sadrabadi, K. M. Cheung, T. D. Young, G. Bahlakeh, A. Moshaverinia, P. S. Weiss, A. M. Andrews, Polyserotonin nanoparticles as multifunctional materials for biomedical applications. *ACS Nano* **12**, 4761–4774 (2018).
51. M. Z. Wrona, G. Dryhurst, Electrochemical oxidation of 5-hydroxytryptamine in aqueous solution at physiological pH. *Bioorg. Chem.* **18**, 291–317 (1990).
52. D. P. Salem, M. P. Landry, G. Bisker, J. Ahn, S. Kruss, M. S. Strano, Chirality dependent corona phase molecular recognition of DNA-wrapped carbon nanotubes. *Carbon* **97**, 147–153 (2016).
53. M. Zheng, V. V. Rostovtsev, Photoinduced charge transfer mediated by DNA-wrapped carbon nanotubes. *J. Am. Chem. Soc.* **128**, 7702–7703 (2006).
54. E. C. Dankoski, R. M. Wightman, Monitoring serotonin signaling on a subsecond time scale. *Front. Integr. Neurosci.* **7**, 44 (2013).
55. F. F. Bergler, F. Schöppler, F. K. Brunecker, M. Hailman, T. Hertel, Fluorescence spectroscopy of gel-immobilized single-wall carbon nanotubes with microfluidic control of the surfactant environment. *J. Phys. Chem. C* **117**, 13318–13323 (2013).
56. W. H. Duan, Q. Wang, F. Collins, Dispersion of carbon nanotubes with SDS surfactants: A study from a binding energy perspective. *Chem. Sci.* **2**, 1407–1413 (2011).

57. Y. Zheng, S. M. Bachilo, R. B. Weisman, Quenching of single-walled carbon nanotube fluorescence by dissolved oxygen reveals selective single-stranded DNA affinities. *J. Phys. Chem. Lett.* **8**, 1952–1955 (2017).
58. J. Budhathoki-Uprety, J. D. Harvey, E. Isaac, R. M. Williams, T. V. Galassi, R. E. Langenbacher, D. A. Heller, Polymer cloaking modulates the carbon nanotube protein corona and delivery into cancer cells. *J. Mater. Chem. B* **5**, 6637–6644 (2017).
59. T. Patriarchi, J. R. Cho, K. Merten, M. W. Howe, A. Marley, W.-H. Xiong, R. W. Folk, G. J. Broussard, R. Liang, M. J. Jang, H. Zhong, D. Dombeck, M. von Zastrow, A. Nimmerjahn, V. Gradinaru, J. T. Williams, L. Tian, Ultrafast neuronal imaging of dopamine dynamics with designed genetically encoded sensors. *Science* **360**, eaat4422 (2018).
60. J. Feng, C. Zhang, J. E. Lischinsky, M. Jing, J. Zhou, H. Wang, Y. Zhang, A. Dong, Z. Wu, H. Wu, W. Chen, P. Zhang, J. Zou, S. A. Hires, J. J. Zhu, G. Cui, D. Lin, J. Du, Y. Li, A genetically encoded fluorescent sensor for rapid and specific in vivo detection of norepinephrine. *Neuron* **102**, 745–761.e8 (2019).

Acknowledgments

Funding: We acknowledge support of NIH NIDA CEBRA award no. R21DA044010 (to M.P.L.), a Burroughs Wellcome Fund Career Award at the Scientific Interface (CASI) (to M.P.L.), the Simons Foundation (to M.P.L.), a Stanley Fahn PDF Junior Faculty Grant with award no. PF-JFA-1760 (to M.P.L.), a Beckman Foundation Young Investigator Award (to M.P.L.), a Radical Ideas grant from the HWNI (to M.P.L.) and a DARPA Young Investigator Award (to M.P.L.). M.P.L. is a Chan Zuckerberg Biohub investigator. This work used the Vincent J. Coates Genomics Sequencing Laboratory at the UC Berkeley, supported by NIH S10 OD018174 Instrumentation Grant. **Author contributions:** S.J. and M.P.L. conceived the ideas of SELEC and designed experiments. S.J. and A.M.M.G. performed the iterative process of SELEC and characterized the nanosensor properties. D.Y. and S.J. analyzed the high-throughput sequencing data. A.G.B. and S.J. carried out ex vivo acute brain slice experiments. S.J., D.Y., A.G.B., A.M.M.G., and M.P.L. discussed the experimental results and wrote the manuscript. All authors discussed the results and commented on the manuscript. **Competing interests:** The authors declare that they have no competing interests. **Data and materials availability:** All data needed to evaluate the conclusions in the paper are present in the paper and/or the Supplementary Materials. Additional data related to this paper may be requested from the authors.

Submitted 13 June 2019
Accepted 30 October 2019
Published 18 December 2019
10.1126/sciadv.aay3771

Citation: S. Jeong, D. Yang, A. G. Beyene, J. T. Del Bonis-O'Donnell, A. M. M. Gest, N. Navarro, X. Sun, M. P. Landry, High-throughput evolution of near-infrared serotonin nanosensors. *Sci. Adv.* **5**, eaay3771 (2019).